International Journal of Fatigue 143 (2021) 106013

Contents lists available at ScienceDirect

International Journal of Fatigue

journal homepage: www.elsevier.com/locate/ijfatigue

Crack initiation behavior and fatigue performance up to very-high-cycle regime of AlSi10Mg fabricated by selective laser melting with two powder sizes

Z.M. Jian [a,b], G.A. Qian [a,b,*], D.S. Paolino [c], A. Tridello [c], F. Berto [d], Y.S. Hong [a,b,*]

[a] State Key Laboratory of Nonlinear Mechanics (LNM), Institute of Mechanics, Chinese Academy of Sciences, Beijing 100190, China
[b] School of Engineering Science, University of Chinese Academy of Sciences, Beijing 100049, China
[c] Department of Mechanical and Aerospace Engineering, Politecnico di Torino, 10129 Turin, Italy
[d] Department of Mechanical and Industrial Engineering, Norwegian University of Science and Technology (NTNU), Richard Birkelands vei 2b, 7491 Trondheim, Norway

ARTICLE INFO

Keywords:
Selective laser melting
AlSi10Mg
VHCF
Defects
Crack initiation

ABSTRACT

The high-cycle and very-high-cycle fatigue (VHCF) behavior of AlSi10Mg specimens manufactured by selective laser melting with different printing powder sizes was investigated. The specimens with 20 μm powder size contained more defects than those with 50 μm powder size, and the latter have a higher fatigue property than the former. Unmelted powders were detected as the main source of crack initiation. The specimens printed with 50 μm powder size are more likely to feature subsurface crack initiation in the VHCF regime. Five different types of crack initiation modes were identified, and the fatigue strength was assessed by statistical model.

1. Introduction

Additive manufacturing (AM) is an advanced manufacturing technology used to produce solid parts by adding discrete layers of materials with computer-aided design (CAD). In contrast to traditional metal-manufacturing processes, AM is an innovative technology for designing new products with unprecedented complexity [1]. ASTM defines AM as "the process of connecting materials from three-dimensional model data to create objects, usually layer by layer, rather than subtraction" [2]. The advantage of AM is that it can be used for manufacturing complex parts and components, which can be directly employed in strategic applications (e.g. in aerospace and biomedical fields). In addition, AM does not require molds, which substantially reduces the cost and increases the flexibility of production of complex components [3]. So far, although AM has been increasingly used, however, very few critical components have been manufactured using it. For the purpose of fully adopting this approach to structural components, it is necessary to properly characterize and understand the mechanical properties of AM-manufactured materials, especially under fatigue loadings.

Among the existing AM methods, selective laser melting (SLM) is a promising approach [4], which has received increasing attention [5]. SLM has been employed for fabricating metallic alloys, such as AlSi10Mg, Ti6Al4V and Inconel 718 [6]. It has been recently reported that the static mechanical properties of SLM metals are better than the counterparts processed by traditional casting [7]. In real production, fatigue damage is the cause of failure of more than 70% of mechanical parts. At present, the main issue associated with SLM is the assessment and estimation of related fatigue performance. In particular, high-cycle fatigue (HCF) and very-high-cycle-fatigue (VHCF) behavior of SLM metals needs to be clearly understood [8–10]. This is true for AlSi10Mg, which is widely utilized in engineering applications.

VHCF is the fatigue damage and failure that occurs after more than 10^7 loading cycles [11]. The earliest reports of fatigue failure beyond 10^7 cycles may date back to the 1960 s. Later, Naito et al. [12] investigated the VHCF behavior of high-strength steels and found the "fish-eye" pattern for the first time. Nishijima et al. [13] reported that the fish-eye pattern was caused by the internal initiation of cracks in the tested specimens. In low-cycle fatigue, only a small fraction of loading cycles is consumed to initiate cracks [14]. However, the crack initiation lifetime in VHCF can be more than 95% of the total fatigue lifetime, which differs completely from that in low- or high-cycle fatigue regimes [15]. In VHCF, cracks start from the interior site of the material, which requires many cycles for propagation [16]. Therefore, it is important to investigate the crack initiation mechanism. Hong et al. [17] proposed the "numerous cyclic pressing" (NCP) model to explain the crack initiation

* Corresponding authors.
E-mail addresses: qianguian@imech.ac.cn (G.A. Qian), hongys@imech.ac.cn (Y.S. Hong).

https://doi.org/10.1016/j.ijfatigue.2020.106013
Received 17 July 2020; Received in revised form 20 October 2020; Accepted 21 October 2020
Available online 26 October 2020

mechanism. Chandran [18] proposed a probability model based on Poisson's distribution, to calculate the probability of surface and internal crack initiation. Many models have been proposed to explain crack initiation, propagation, and lifetime prediction of VHCF, such as the Murakami [19], Beretta [20], and Hong models [21]. A discussion on some other fundamental findings related to VHCF can be found in [22–25].

Some recent investigations have been carried out on aluminum and titanium alloys manufactured by SLM, and the corresponding manufacturing parameters have been studied. Srinivasa et al. [26] investigated the effects of the working environment and built-in orientation on the static mechanical properties of AlSi10Mg, showing that the cost-effectiveness of nitrogen as a protective gas is better than that of argon. Uzan et al. [27] investigated the effect of shot-peening on fatigue crack initiation sites, showing that the location of crack initiation is deeper than that in the specimens without shot-peening. Nesma et al. [28] studied the effect of powder parameters on density or porosity of AlSi10Mg manufactured using SLM. Tradowsky et al. [29] investigated the heat treatment effect on the fatigue properties of AlSi10Mg and found that the combination of platform heating temperature at 300 °C and T6 heat treatment is an effective method for improving the fatigue strength. Nadot et al. [30] investigated the effect of defect size on the HCF properties of AlSi10Mg, showing which defects do not affect the final fatigue strength. Uzan et al. [31] investigated the mechanical property of AlSi10Mg at high temperatures, and found that plastic deformation occurs during creep. Rosenthal et al. [32] reported that the fatigue property of AlSi10Mg is very sensitive to the strain rate. Read et al. [33] studied the effect of cooling rate on the fatigue property of AlSi10Mg and found that the defect morphology during the fatigue damage process is not sensitive to the cooling rate. As for titanium alloy, the corresponding mechanical and fatigue properties have been studied. Bastien et al. [34] investigated the effects of the surface roughness of Ti-6Al-4 V parts produced by SLM on HCF behavior, showing that the HCF life is significantly reduced due to the effect of surface roughness. Victor et al. [35] compared the fatigue properties of Ti-6Al-4 V specimens fabricated by EBM and SLM, indicating that the machined specimens have better fatigue property with the elimination of surface defects. Dzugan et al. [36] investigated the effect of the orientation and thickness of Ti-6Al-4 V samples on its microstructures and tensile properties, showing that the microstructures and mechanical properties are related to the direction of construction, and partly to the thickness and location of the samples in the cavity. Beevers et al. [37] investigated the influence of AM processing parameters and possible resulting imperfections on the fatigue behaviour of an AlSi10Mg alloy. In practical production, HT (heat treatment) is the most common method to improve the mechanical properties of AM parts. AlSi10Mg alloys manufactured by SLM usually have higher strength, but relatively poor ductility. Therefore, the microstructure of AlSi10Mg alloy can be improved by the HT process, thus improving the fatigue property. Normally, post HT may enhance the ductility of the builds but may reduce the strength of Al-Si alloys. The post HT is also used to reduce the porosity of AM parts, thus lessening the potential locations of crack initiation and improving the fatigue performance. Han et al. [38] investigated the effect of post-treatment on the microstructure and mechanical properties of an AlSi10Mg manufactured by SLM, showing that the tensile strength of the AlSi10Mg alloy is reduced and the plasticity is improved by HT thanks to the resulted grain growth and the release of residual stress. In general, the fatigue properties of the AlSi10Mg manufactured by SLM can be improved by appropriate HT process. Other relevant contributions dealing with SLM technology and the mechanical properties of materials that are manufactured by this technology have been recently published [39–52]. However, only a few studies have been carried out to address the VHCF performance of the components manufactured by SLM. Therefore, this paper aimed at partially filling this gap, by investigating the VHCF property of AM parts, which will be of significant interest for many industrial applications with the design knowledge of safer products and components.

In this paper, both HCF and VHCF behavior of AlSi10Mg made by SLM was studied. The effect of different powder sizes on the fatigue property and crack initiation characteristics was studied. Three different loading ratios ($R = -1, 0, 0.5$) were adopted in the ultrasonic fatigue testing (f = 20 kHz). Scanning electron microscopy (SEM) was used to observe fracture surfaces and a three-dimensional (3D) white light interferometer was used to measure the fracture surface roughness. Moreover, the VHCF strength of the specimens fabricated by SLM was evaluated in terms of P-S-N curves (probabilistic fatigue-life or, equivalently, P-S-N curves are defined by a probabilistic model and used to assess the fatigue strength of the tested specimens) with a statistic analysis.

2. Material and specimens

In this section, material, specimen design, SLM process and related processing parameters are described.

2.1. Material

AlSi10Mg specimens for tensile and fatigue tests were manufactured by SLM. The chemical composition of the material is listed in Table 1.

2.2. Selective laser melting process

The laser power of the present SLM processing was 370 W. The scanning speed was 1300 mm/s and the scanning spacing was 0.19 mm. In the process of actual production, the metal powder melts and solidifies rapidly to form one layer of the component. The base drops one layer after scanning and the powder pool feeds the powder. Then, the required specimens with two kinds of powder size (20 μm, 50 μm) were produced (without post heat treatment). The specimens printed with a powder size of 20 μm are named as Group A and the specimens printed with a powder size of 50 μm are names as Group B. It is important to choose whether to add a support structure according to the geometric characteristics of the component. In fact, printing at 0° (horizontal) means pushing the components down without adding a support structure. During the descent of the base, the scraper scrapes back and forth two times. The first pass is necessary for scraping the unmelted powder away, while the second pass seeks to determine the powder size. The rigid scraper scrapes the metal powder from the powder pool. The related SLM processing parameters used in this paper are listed in Table 2.

2.3. Specimen design

The stress distribution of ultrasonic fatigue specimens satisfies the one-dimensional wave equation with variable cross-section [53]. Based on the calculation, the geometry of the specimens for the monotonic quasi-static tensile test is shown in Fig. 1a, and the geometry of the specimens for the fatigue test is shown in Fig. 1b. The density of Group A is 2.475 ± 0.001 g/cm^3 and the density of Group B is 2.538 ± 0.001 g/cm^3. Besides, the length in relation to the control area (with respect to the 90% of the subjected stress) of the fatigue specimen is 0.59 mm and that of tensile specimens is 56 mm. The specimens were prepared by cutting from the bulk material, which are originally in cylindrical shape manufactured by SLM. The surface of specimen was polished before the tests were conducted.

3. Experimental procedure

3.1. Tensile tests

The design of the AlSi10Mg tensile test specimens, as shown in Fig. 1a, was in accordance to Chinese code of GB/T228-2002. For each

Table 1
Nominal chemical composition of the tested AlSi10Mg specimens (wt. %).

Element	Al	Si	Mg	Fe	Ti	Cr	Cu	Mn	Ni	V	Zn
wt. %	Balance	9.75	0.22	0.092	0.011	<0.01	<0.01	<0.01	<0.01	<0.01	<0.01

Table 2
SLM manufacturing parameters of the analyzed AlSi10Mg specimens.

Laser power [W]	Scanning speed [mm/s]	Scanning spacing [mm]	Preheating temperature[°C]	Layer thickness[mm]	Printing direction [°]	Laser profile
370	1300	0.19	35	0.02, 0.05	0	Gaussian

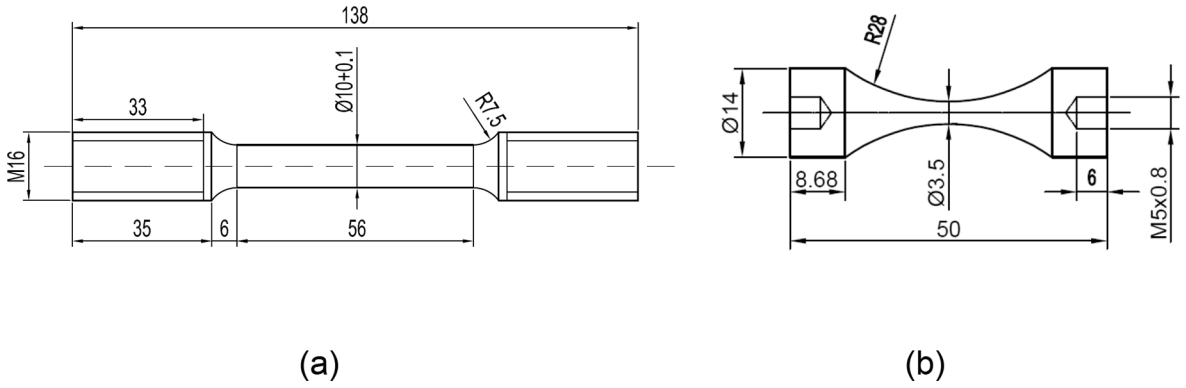

Fig. 1. Geometry of (a) tensile test specimens under monotonic quasi-static loading, and (b) fatigue test specimens under ultrasonic axial cycling (dimensions in mm).

group of specimens printed with different powder sizes, six specimens were tested at a tension rate of 2 mm/min.

3.2. Ultrasonic fatigue tests

An ultrasonic fatigue machine with a resonance frequency of 20 kHz was used for the present fatigue tests. The experiments were carried out by the displacement control in the range between 2.2 μm and 21.5 μm. According to the stress–strain relationship, the stress range was between 40 MPa and 390 MPa. The AlSi10Mg specimens with two kinds of powder size (20 μm, 50 μm) under three stress ratios ($R = -1, 0, 0.5$) were used in the experiment. Ten specimens were tested under each stress ratio.

3.3. Roughness measurements

The roughness of specimen may affect fatigue crack initiation. In this experiment, the surface roughness of the AlSi10Mg specimens was measured by using a 3D white light interferometer, and the effect of the roughness on the VHCF properties was investigated by statistical analysis.

4. Results and discussion

This section gives the tested results and discusses the stress–strain curve, microstructure, S-N curve, fractography, roughness and hardness measurements, as well as fatigue strength evaluations.

4.1. Engineering stress–strain curve

The monotonic quasi-static tensile stress–strain curves are summarized in Fig. 2. Yield strength (YS), ultimate tensile strength (UTS) and elongation are listed in Table 3. It is seen that the elongation of Group B is obviously better than that of Group A. However, no large difference on the elastic modulus of the specimens is observed. The possible reason is that the smaller the powder size is, the larger the defect is. The elongation mainly depends on the defect size, so the elongation of Group B is higher.

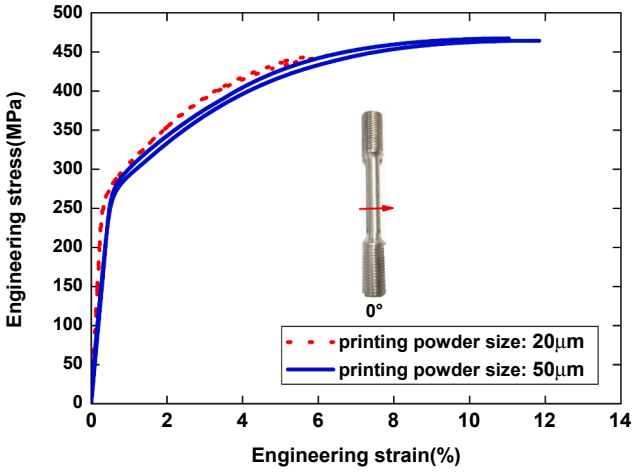

Fig. 2. Engineering stress versus strain, for specimens with different printing powder sizes.

Table 3
Tensile properties of the AlSi10Mg specimens.

	YS (MPa)	UTS (MPa)	Elongation (%)
Group A (20 μm)	276 ± 4	445 ± 6	6.1 ± 0.5
Group B (50 μm)	280 ± 4	465 ± 6	11.8 ± 0.5

4.2. Microstructure

In sections D1 and D2, as shown in Fig. 3, material microstructures were observed. The morphologies in sections D1 and D2, for Group B are shown in Fig. 3(a) and (b). Fig. 3(a) shows the microstructure along the direction of section D1 and the arrow points to some unfused defects, which were formed as several unmelted areas in the melt pool became connected during the sweeping process. Fig. 3(b) shows the microstructure along direction of section D2; the holes and the direction of laser scanning arranged alternately in a long strip are observed. It is obvious that the microstructures of sections D1 and D2 are quite different under the same printing method. These observations clearly confirm the anisotropic microstructure of the specimens manufactured by SLM. As will be presented in Section 4.3, the fatigue property of Group B is better, which is attributed to their material microstructure. In contrast, Fig. 3(c) shows that Group A contains more pores and larger defect areas. By comparing Fig. 3(a) with Fig. 3(c), it is found that this is a general result. The reasons may be as follows: first, the finer particles have worse powder fluidity which results in higher porosity under SLM process. Secondly, a relatively larger surface area of the finer particles leads to more H_2O sorption/desorption conjugated with H_2 formation which also may cause high porosity level. In addition, Fig. 3(c) shows that the defect size of Group A is of the same size as the melt pool. Thus, the defects and pores degrade the fatigue property significantly, especially in the crack initiation and early propagation stages. The defects and pores will be the locations of stress concentration in the specimen, which will be the hot spots of crack initiation and lower the fatigue strength. In addition, the effects of the shape, size and location of defects on fatigue properties are investigated in [54]. Defect density distributions for the specimens manufactured with different powder sizes are further quantified in Fig. 3(d). For Group A, the defect size distribution is wider and extends toward higher values, compared with the distribution for Group B. The average defect radius for Group A is larger than Group B, which results in the decreasing of fatigue properties. This is an explanation for the increase of fatigue property with increasing powder size, which will be described in the following section.

In Fig. 4, an amplified view of the microstructure image of Group B shows the morphology of the melt pool. The fine grain area consists of smaller size grains, the coarse grain area is with larger size grains, and the heat-affected zone is with sparse grain distribution. By magnifying the microstructure image of Group B, the morphology of the melt pool is shown clearly and the laser scanning trace is shown in Fig. 4 along the directions of sections D1 and D2.

4.3. VHCF performance: S-N data

Two groups of AlSi10Mg specimens were used in the fatigue testing. The S-N data are summarized in Fig. 5. It is observed that the fatigue properties of Group B are obviously better, for all three different stress ratios ($R = -1, 0, 0.5$). With the decrease of Group A, the fatigue lifetime decreases, and the scatter of the fatigue data for Group A is larger (when $R = 0, 0.5$). The mean stress also plays an important role in the fatigue property of the AlSi10Mg specimens. It is visible from Fig. 5 that the fatigue strength decreases with the increase of mean stress, which is consistent with the common practice. The fatigue properties in terms of stress amplitude for Group B and tested at $R = -1$ are better than those for the specimens tested at $R = 0$ and 0.5. One possible reason is that for $R = -1$, the pore closure occurs owing to the reverse compression, which improves the fatigue properties. For $R = 0$ and 0.5, the mean stress is a positive value, and the porosity continuously increases under cyclic loading, reducing the fatigue strength. Deeper understanding of the effect of mean stress on the fatigue strength is still needed.

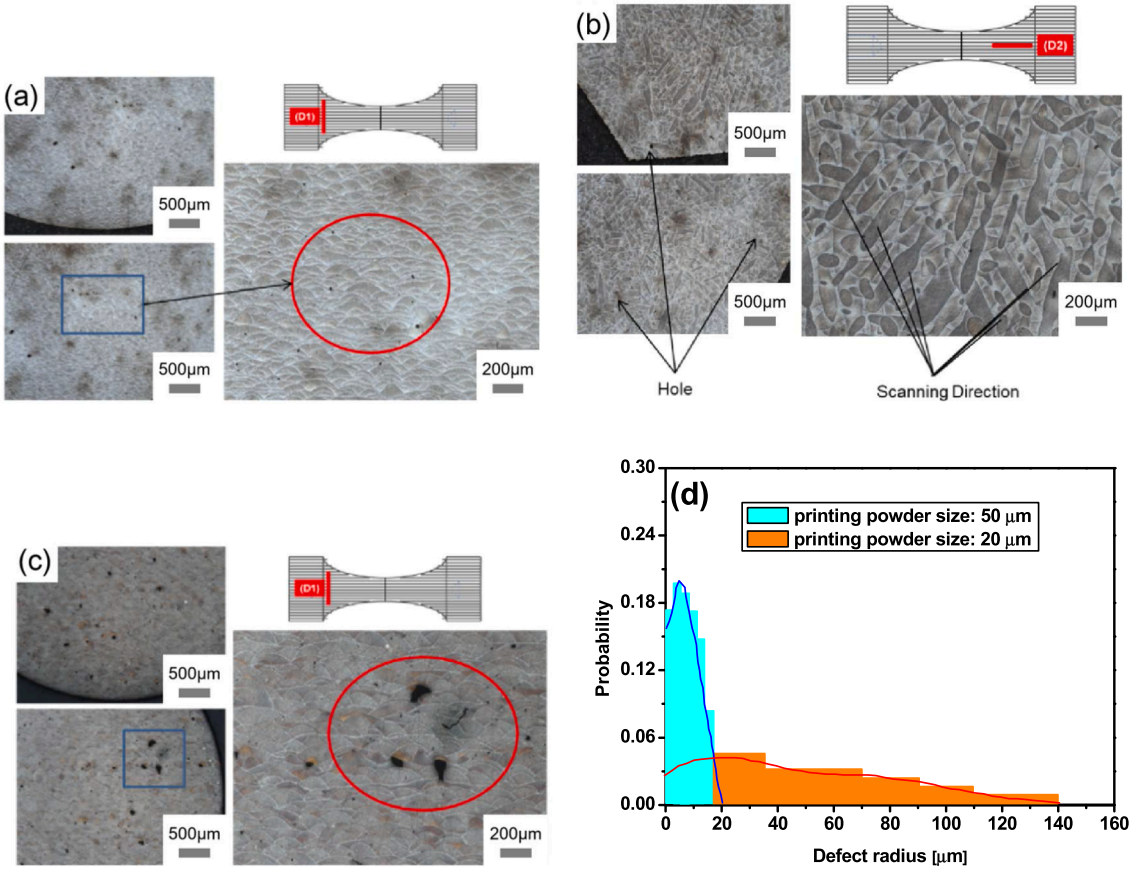

Fig. 3. (a) Microstructure of the specimens printed with a powder size of 50 μm in section D1; (b) printed with a powder size of 50 μm in section D2; (c) printed with a powder size of 20 μm in section D1;(d) defect density distributions for the specimens printed with powder sizes of 50 μm and 20 μm.

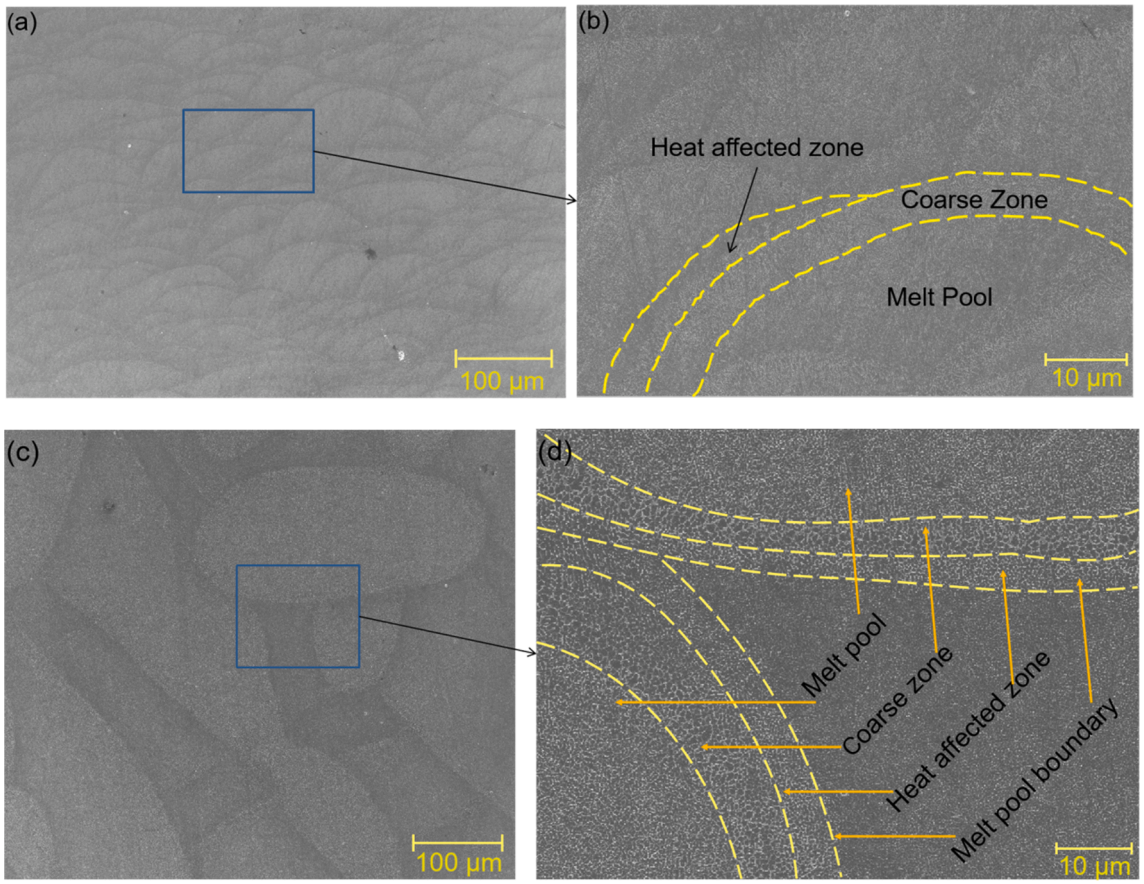

Fig. 4. Microstructure of the specimens printed with a powder size of 50 μm (a) and (b) from section D1; (c) and (d) from section D2.

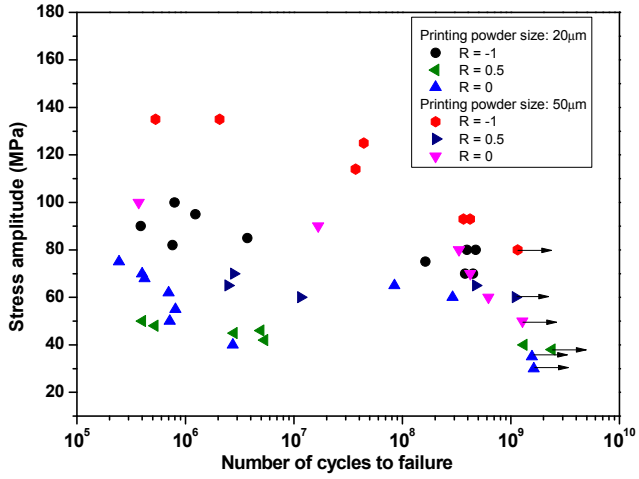

Fig. 5. S-N data for the specimens manufactured with different powder sizes, tested at different stress ratios.

It is evident that defects play an important role in the fatigue crack initiation. After observing the fracture surfaces of tested specimens by SEM, four types of defects in the tested AlSi10Mg specimens were detected: (a) unfused defects, which are formed between the melt pools during laser scanning; (b) inclusions, which are formed during specimen preparation, as a small amount of Al binds to oxygen, forming Al_2O_3; (c) porosity defects, which emerge during specimen preparation when the existing voids are not scanned; and (d) unmelted powders, which occur when the metal powders are not completely melted, because of the insufficient input energy.

4.4. Fractography

The fracture morphology observations by SEM are summarized in this section, so as to study the characteristics of fatigue crack initiation.

An essential difference between HCF and VHCF is that the crack initiation site switches from the surface to the subsurface or bulk of specimen. The fracture surface is usually divided into three regions—crack initiation area, propagation zone and fracture zone. It is shown in Fig. 6 (a) that HCF cracks originate from the surface, while Fig. 6 (b) shows that internal crack initiation is dominant for VHCF. A fisheye pattern is also observed for VHCF.

Based on the fracture surface observations via SEM, the origin of fatigue cracks can be summarized into the following five types, as shown in Fig. 7(a) Surface origin: When the stress amplitude, loading ratio and mean stress are high, the influence of the surface roughness on the fatigue crack initiation is dominant. The surface roughness of the SLM-prepared AlSi10Mg specimens varies greatly, which makes it easier to cause stress concentration, thus inducing the surface crack origin. (b) Sub-surface origin: The crack initiation site is located between surface and bulk but belongs to the bulk. (c) Internal origin: When the stress amplitude is low, the sensitivity to the surface roughness decreases, and the fatigue crack initiation is more inclined to occur on the interior of specimen. (d) Internal flaws: The existence of defects (four kinds) leads to different degrees of stress concentration in the specimen, which affects the fatigue lifetime and the final strength under cyclic loadings. (e) Melt pool type: The morphology and the size of crack initiation area are similar to those of the melt pool; thus, “melt pool type defects” play a key role in the fatigue crack initiation. It is worth noticing that in the crack initiation region, a fine granular area and a fisheye pattern are observed, as shown in Fig. 7. The structure, formation of this fine granular area and the crack initiation mechanism needs to be further investigated (see

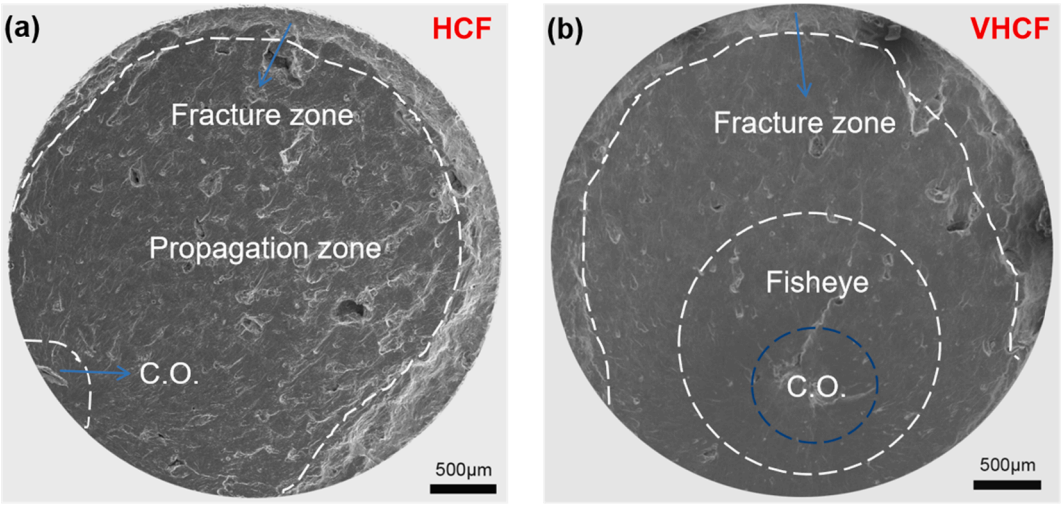

Fig. 6. Fracture surface morphology of the specimens manufactured with a powder size of 20 μm in HCF and VHCF:(a)R = 0, σ_a = 40 MPa and N = 2.74x10^6;and (b) R = -1, σ_a = 70 MPa and N = 4.48x10^8.C.O. : crack origin.

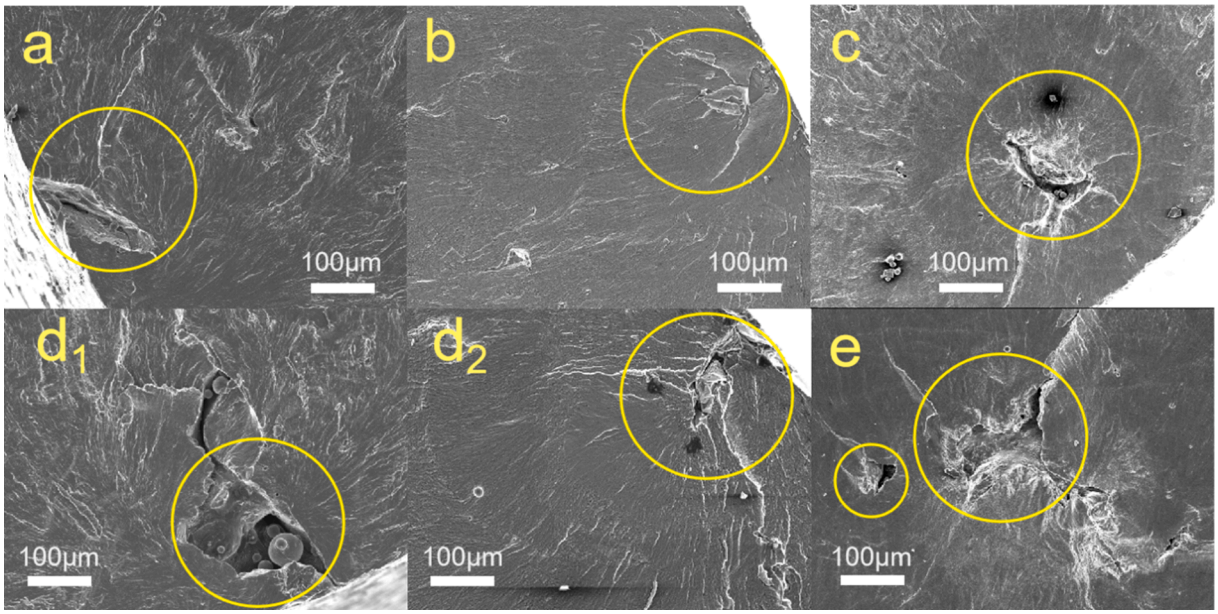

Fig. 7. Five types of crack origins: (a) Surface origin (20 μm, R = 0, σ_a = 40 MPa, and N = 2.74x10^6); (b) sub-surface origin (50 μm, R = 0, σ_a = 90 MPa, and N = 1.68x10^7); (c) internal origin (20 μm, R = 0, σ_a = 60 MPa, and N = 2.90x10^8); (d_1) "defect origin" (20 μm, R = 0.5, σ_a = 48 MPa, and N = 5.23x10^5); (d_2) "defect origin" (50 μm, R = 0, σ_a = 100 MPa, and N = 3.72x10^5);(e) "melt pool type" (20 μm, R = -1, σ_a = 70 MPa, and N = 4.48x10^8).

Fig. 8).

From the observations of the S-N data, one possible reason for the weak fatigue performance can be that Group A contain a large number of defects, as shown in Fig. 3(c). By summarizing a large number of fatigue fracture surfaces, it was found that unmelted powders are the contributors to crack origination in Group A. This is owing to the fact that a large number of crack initiation sites contain unfused powders of the same magnitude as the crack origin region. It is noted that Group A contain a large number of defects than Group B.

The melt pool size has a key influence on the fatigue crack initiation, so the size and the depth of crack origin area are discussed below using statistical considerations. The crack origin and its depth are shown in Fig. 9(a) and (b), respectively. In order to illustrate the position of crack initiation in VHCF, the fracture surface under SEM is treated as a circle, and then the crack initiation region of VHCF is reflected on the circle. It seems from the data points plotted in Fig. 10(a) that the crack initiation position of Group A under VHCF is closer to the edge of equivalent fracture surface, whereas the cases of Group B are more likely to feature subsurface crack initiation sites, according to the statistics of the crack origin depth and the fracture morphology.

The sizes of the defects that led to the fatigue failures were also analyzed. According to the literature [44,55], the initial defect size, $\sqrt{area}$, is assumed to follow a Largest Extreme Value (LEV) distribution. In Fig. 10(b), the $\sqrt{area}$ values are reported on a Gumbel plot, together with the estimated LEV distributions. The parameter estimation has been carried out by applying the Maximum Likelihood Principle.

According to Fig. 10(b), the size of the defects that caused fatigue failures increases with the decreasing of the powder size from 50 μm to 20 μm. The largest critical defect in the specimens produced with the powder size of 50 μm is about 110 μm. On the other hand, 8 out of 25 defects in the specimens produced with the powder size of 20 μm are larger than 110 μm, with the largest defect characterized by $\sqrt{area}$ of

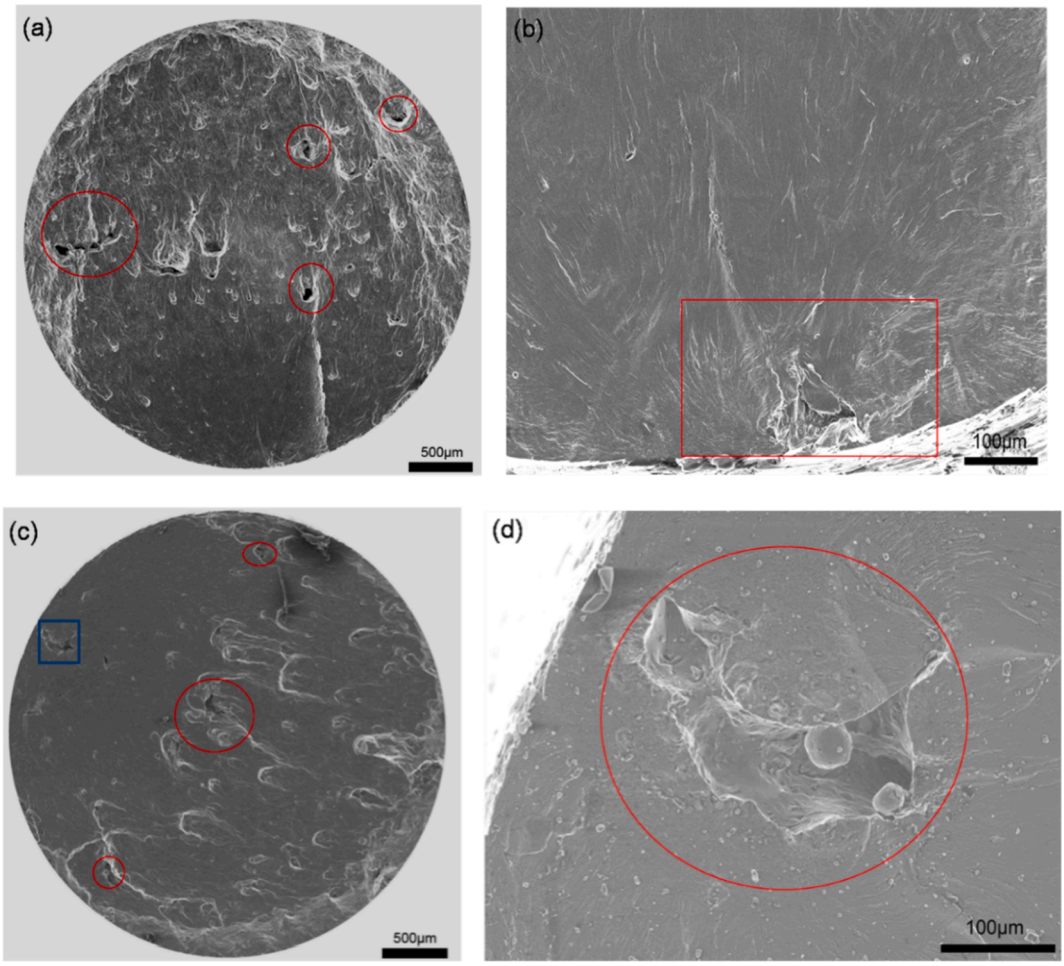

Fig. 8. Unmelted powders in HCF and VHCF specimens :(a) unmelted powders of 20 μm, R = -1, σ_a = 100 MPa, and N = 7.94x10^5; (b) crack origin zone of (a); (c) unmelted powders of 20 μm, R = -1, σ_a = 80 MPa, and N = 3.93x10^8; and (d) crack origin zone of (c).

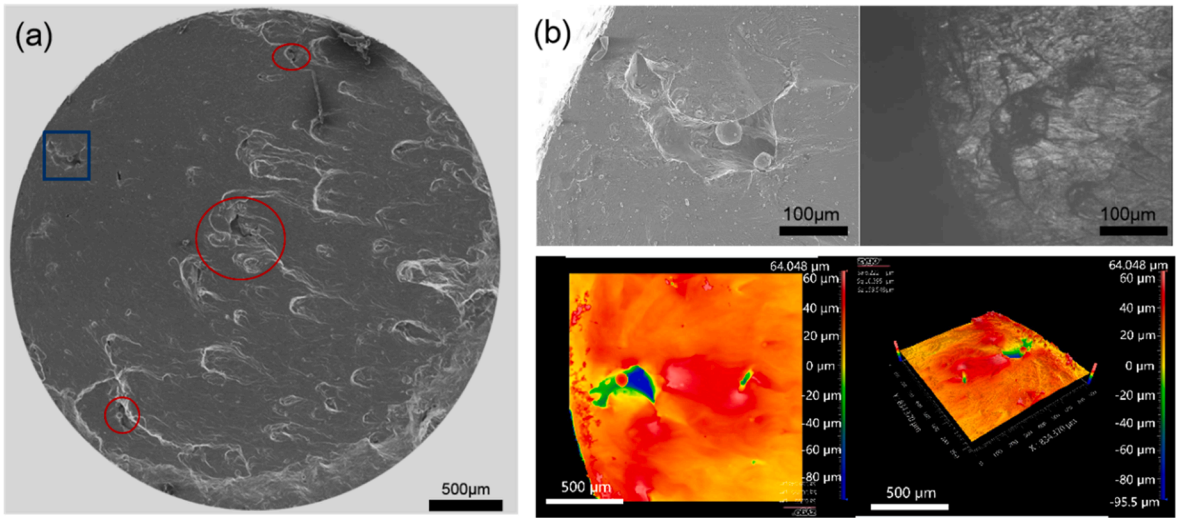

Fig. 9. Crack origin depth (20 μm, R = -1, σ_a = 80 MPa, and N = 3.93x10^8).

about 200 μm. The influence of the defect size on the VHCF response will be investigated in Section 4.7 by comparing the P-S-N curves and the VHCF strength at $N = 10^9$ cycles.

4.5. Surface roughness and Vickers hardness

Surface roughness has a significant effect on the fatigue property of AlSi10Mg specimens. In many cases, HCF occurs owing to a large surface roughness, which leads to the stress concentration on the surface and

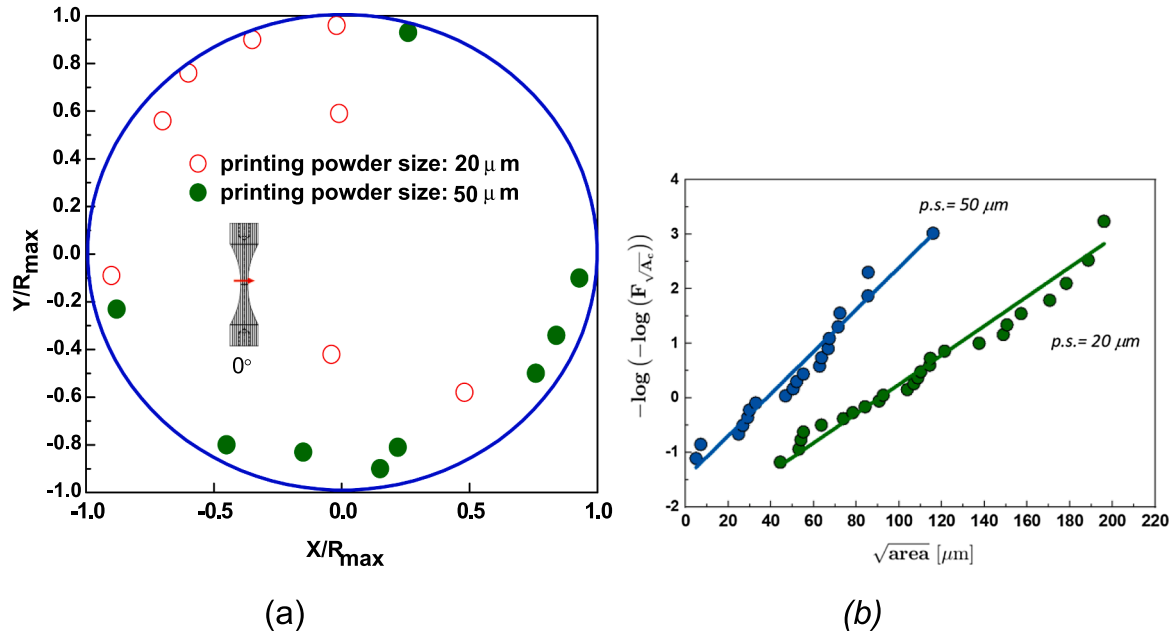

Fig. 10. (a): Statistical presentation of crack origin (in VHCF); (b): Gumbel plot of the initial defect sizes and estimated LEV distributions for specimens produced with powder size of 50 μm and 20 μm.

surface crack initiation. In general, the greater the surface roughness is, the easier it is for the stress concentration to form crack initiation sites, thus reducing the fatigue lifetime.

The average surface roughness in the control area was measured. The average surface roughness was $R_a = 2.746$ μm for Group A, and it was 2.526 μm for Group B, as shown in Fig. 11(a). The left panel in Fig. 11(a) shows the physical picture of the optical lens in the middle of the sample. The right panel in Fig. 11(a) shows the 3D view, obtained after flattening the 3D area, which makes the measured value effective. Even though the average surface roughness for Group A is higher, the difference between the two groups is small and cannot be the reason for a different fatigue response. When the areas with significant surface roughness are abundant, the surface roughness values for the same specimen at different locations of the same cross-section are quite different, which leads to a larger dispersion of fatigue strength.

The Vickers hardness of the two types of specimens was measured equidistantly along the same radial direction and the representative results are shown in Fig. 11(b). The average HV for Group A was 122 kgf/mm^2, while the average HV for Group B was 132 kgf/mm^2. Even though the difference in the hardness values is limited, it still can partially explain the different mechanical and fatigue properties between the two groups. The Vickers hardness will be used for the fatigue strength calculation in the next section.

4.6. Experimental stress amplitude assessment by Murakami model

In this section, the Murakami model [54] was employed to assess the experimental stress amplitude for the failure cases due to surface and internal crack origins. In the Murakami model, it was assumed that there is a control region in the fatigue specimen. The fatigue crack initiation

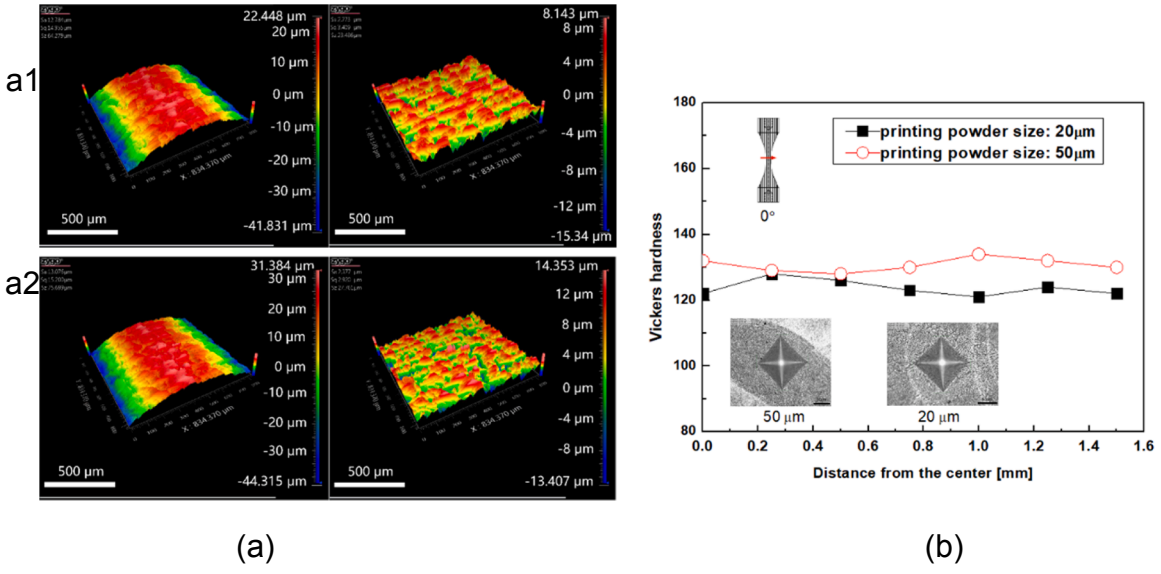

Fig. 11. (a): Surface roughness :(a1) a specimen printed with a powder size of 20 μm, and (a2) a specimen printed with a powder size of 50 μm; (b): Vickers hardness distributions in specimen radial direction.

has a certain probability in the control region. The schematic diagram of the crack initiation area in the Murakami model is shown in Fig. 12(a). The experimental stress amplitude was calculated by measuring the crack initiation area.

The threshold stress intensity factor range ΔK_{th} can be evaluated by Eq. (1), and the fatigue limit can be evaluated by Eq.(2) [55,56]:

$$\Delta K_{th} = \frac{3.3 \times 10^{-3}(HV + 120)}{\sqrt[1/6]{area}} \quad (1)$$

$$\sigma_w = 1.43\frac{(HV + 120)}{\sqrt[1/6]{area}} \quad (2)$$

where HV is the hardness, R is the stress ratio, and "area" represents the projection area of the crack origin on the plane perpendicular to the loading axis. More general expressions for Eq. (1) and Eq. (2) are shown in Eqs. (3) and (4), for surface and internal defects, respectively [55,56].

Surface defects:

$$\sigma_{surface} = 1.43\frac{(HV + 120)}{\sqrt[1/6]{area}}\left(\frac{1 - R}{2}\right)^{\alpha} \quad (3)$$

Internal defects:

$$\sigma_{internal} = 1.56\frac{(HV + 120)}{\sqrt[1/6]{area}}\left(\frac{1 - R}{2}\right)^{\alpha} \quad (4)$$

where $\alpha = 0.226 + HV \times 10^{-4}$

ImageJ software was used to measure the surface and internal crack areas. The hardness HV and stress ratio R were inserted into Eqs. (3) and (4) to calculate the experimental stress amplitude. The assessed stress amplitude versus experimental stress amplitude is shown in Fig. 12(b). The predicted stress amplitude and the experimental stress amplitude are basically linearly correlated with a relatively small error, which means that the obtained stress amplitudes can be predicted by the Murakami model. Note that here the original Murakami model is adopted for the sake of generality although some modified models in relation to specific experimental conditions and/or materials were proposed in the literature.

4.7. P-S-N curves: The effect of powder size

In this section, the P-S-N curves and the VHCF strength at $N = 10^9$ cycles are estimated and compared so as to assess the effect of the powder size on the VHCF response [56–58]. Since the VHCF tests were carried out at different stress ratios (i.e., –1, 0, and 0.5), an equivalent stress amplitude at $R = -1$ was computed for the specimens tested at $R = -1$. This permitted to increase the number of experimental data for the estimation of the P-S-N curves and to more properly assess the effect of powder size. In particular, the equivalent stress amplitude for different stress ratios, $s_{a,eq}$, was computed according to the "Smith-Watson-Topper" (SWT) model [59]:

$$s_{a,eq} = s_{max} \cdot \sqrt{\frac{1 - R}{2}} \quad (5)$$

where s_{max} is the maximum applied stress during a load cycle.

The marginal P-S-N curves were considered for the comparison: "marginal" since they were estimated by also considering the defect size distribution, which was affected by the powder size (Fig. 10b).

For the specimens produced with the powder size (p.s. in the following) of 50 μm, a monotonic linear decreasing model was considered for the estimation of the P-S-N curves:

$$F_Y(y;x) = \int_0^{\infty} F_{Y|\sqrt{area}}\left(\frac{y - \mu_Y(x,\sqrt{area})}{\sigma_Y}\right) f_{\sqrt{A}}\left(\frac{\sqrt{area} - \mu_{\sqrt{A}}}{\sigma_{\sqrt{A}}}\right) d\sqrt{area} \quad (6)$$

where $F_Y(y;x)$ is the cumulative distribution function (cdf) of the finite fatigue life $Y = \log_{10}[N]$ (i.e. the fatigue life is the logarithm of the number of cycles to failure, N), with $x = \log_{10}[s_{a,eq}]$; $F_{Y|\sqrt{area}}\left(\frac{y-\mu_Y(x,\sqrt{area})}{\sigma_Y}\right)$ is the cdf of the conditional finite fatigue life $Y|\sqrt{area}$ (i.e. the finite fatigue life for a given initial defect size), with $\mu_Y(x,\sqrt{area}) = c_Y + m_Y x + n_Y \log_{10}[\sqrt{area}]$ and σ_Y a constant parameter; $f_{\sqrt{A}}\left(\frac{\sqrt{area}-\mu_{\sqrt{A}}}{\sigma_{\sqrt{A}}}\right)$ is the probability density function (pdf) of the initial defect size $\sqrt{A}$, with $\mu_{\sqrt{A}}$ and $\sigma_{\sqrt{A}}$ two constant parameters.

Typically, the fatigue life follows a Normal distribution (i.e. the number of cycles to failure N follows a LogNormal distribution) with

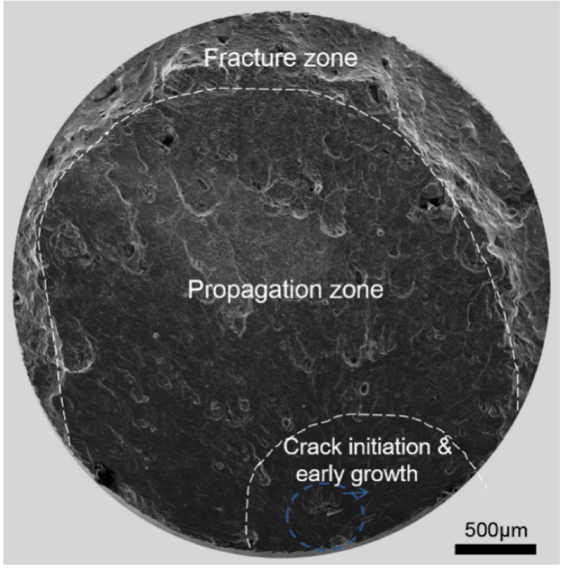

(a)

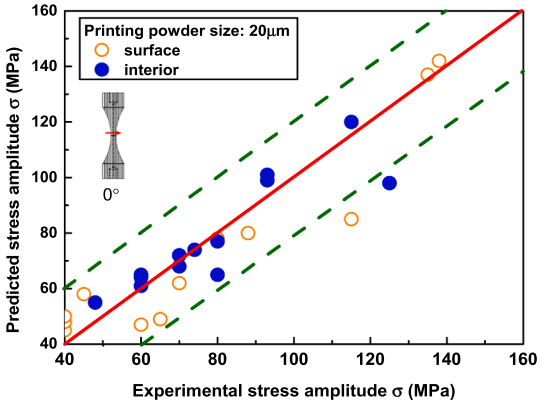

(b)

Fig. 12. (a): Fracture morphology of HCF (20 μm, R = 0, σ_a = 75 MPa, and N = 2.45x10^6); (b): Fatigue strength predicted by Murakami model vs. experimental data: (20 μm, R = 0).

mean $\mu_Y(x, \sqrt{area})$ and standard deviation σ_Y, and the initial defect size follows a LEV distribution with parameters $\mu_{\sqrt{A}}$ and $\sigma_{\sqrt{A}}$, according to Section 4.4:

$$F_Y(y;x) = \int_0^{\infty} \Phi\left(\frac{y-\mu_Y(x,\sqrt{area})}{\sigma_Y}\right) \frac{\varphi_{LEV}\left(\frac{\sqrt{a_{d0}}-\mu_{\sqrt{A}}}{\sigma_{\sqrt{A}}}\right)}{\sigma_{\sqrt{A}}} d\sqrt{area} \quad (7)$$

Since no runout specimens were present, the constant coefficients of the mean fatigue life and the standard deviation have been estimated through a multiple linear regression. The α-th quantile of the P-S-N curve has been estimated by solving Eq. (6) with respect to x for different values of y and by considering $F_Y(y;x) = \alpha$.

For the specimens produced with powder size of 20 μm, the model of "*two failure modes separated by a transition stress*" [39] has been considered for the estimation of the P-S-N curves:

$$F_Y(y;x) = F_{Y,HCF}(y;x) \cdot F_{X_t}\left(\frac{x-\mu_{X_t}}{\sigma_{X_t}}\right) + F_{Y,VHCF}(y;x) \cdot \left(1 - F_{X_t}\left(\frac{x-\mu_{X_t}}{\sigma_{X_t}}\right)\right) \quad (8)$$

where $F_{Y,HCF}(y;x) = \int_0^{\infty} \Phi\left(\frac{y-\mu_{Y,HCF}(x,\sqrt{area})}{\sigma_{Y,HCF}}\right) \frac{\varphi_{LEV}\left(\frac{\sqrt{a_{d0}}-\mu_{\sqrt{A}}}{\sigma_{\sqrt{A}}}\right)}{\sigma_{\sqrt{A}}} d\sqrt{area}$ is the marginal cdf of the finite fatigue life in the HCF region (estimated from Eq. (7) by only considering the fatigue failures below 10^7 cycles), $F_{Y,VHCF}(y;x) = \int_0^{\infty} \Phi\left(\frac{y-\mu_{Y,VHCF}(x,\sqrt{area})}{\sigma_{Y,VHCF}}\right) \frac{\varphi_{LEV}\left(\frac{\sqrt{area}-\mu_{\sqrt{A}}}{\sigma_{\sqrt{A}}}\right)}{\sigma_{\sqrt{A}}} d\sqrt{area}$ is the marginal cdf of the finite fatigue life in the VHCF region (estimated from Eq. (7), by only considering the fatigue failures beyond 10^7 cycles) and $F_{X_t}\left(\frac{x-\mu_{X_t}}{\sigma_{X_t}}\right)$ is the cdf of the transition fatigue stress, with μ_{X_t} and σ_{X_t} being two constant parameters. According to Ref. [39], the transition stress was assumed to follow a LogNormal distribution with parameters μ_{X_t} and σ_{X_t}.

The constant coefficients of the mean fatigue life and of the standard deviation in the HCF and the VHCF regimes have been estimated separately through a multiple linear regression. The constant coefficients of the LEV distribution have been estimated through the application of the Maximum likelihood principle by considering one LEV distribution for √area, regardless of the fatigue regime (no distinction between HCF and VHCF), according to Fig. 10b. Finally, the mean and the standard deviation of the transition stress were estimated through the application of the Maximum Likelihood Principle by considering Eq. (8) and both failures and runout specimens.

The estimated median, the 0.025-th and the 0.975-th quantiles (95% confidence interval) of the P-S-N curves for AlSi10Mg specimens with powder size of 50 μm and with powder size of 20 μm are shown in Fig. 13 (a) and (b), respectively.

Once the P-S-N curves were estimated, for a proper and reliable assessment of the effect of the powder size on the VHCF strength, the pdf and the cdf of the VHCF strengths at $N = 10^9$ cycles were compared. The pdf of the VHCF strengths at $N = 10^9$ cycles were estimated by considering $y = \log_{10}[10^9]$ and by solving Eq. (6) (powder size of 50 μm) and Eq. (8) (powder size of 20 μm) for different values of y. The cdf for the specimens produced with powder size of 50 μm and 20 μm has been estimated from Eqs. (6) and (8), by considering $y = \log_{10}[10^9]$ and by simulating 10,000 values of × with the Monte Carlo method. In order to

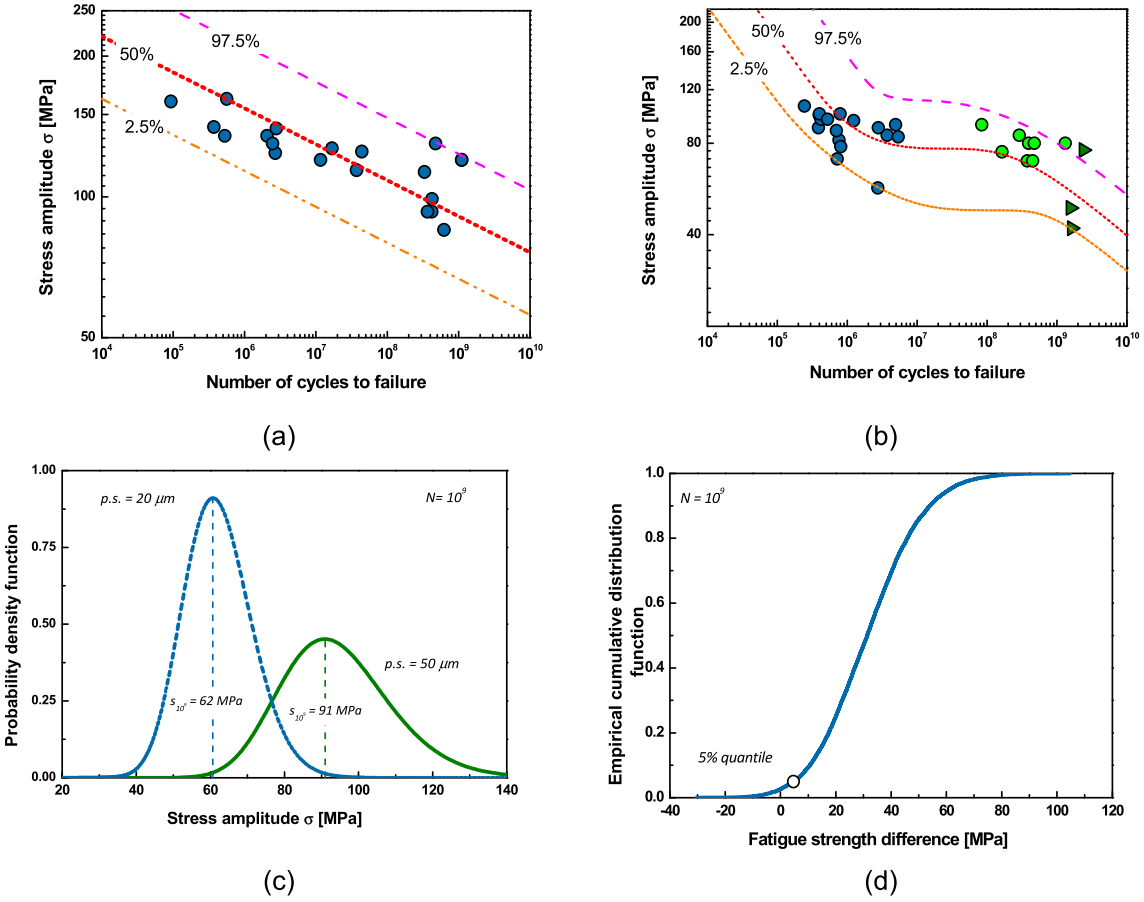

Fig. 13. (a) Estimated P-S-N curves for AlSi10Mg specimens with powder size equal to 50 μm; (b) powder size equal to 20 μm; (c) statistical assessment of the effect of powder size on VHCF strength at N = 10^9 cycles with pdfs for VHCF strengths; (d) ecdf for the difference between the VHCF strengths.

assess if the difference between the VHCF strengths is statistically significant, the empirical cumulative distribution function (ecdf) of the difference has been computed and the confidence interval analysed.

Fig. 13(c) compares the pdf of the VHCF strengths at $N = 10^9$ cycles for the specimens produced with the powder size of 50 μm and 20 μm. Fig. 13(d) shows the ecdf of the difference between the VHCF strength at $N = 10^9$ cycles. Fig. 13(c) confirms that the powder size significantly influences the VHCF strength: in particular, by decreasing the powder size from 50 μm to 20 μm, the median value of the VHCF strength decreases from 91 MPa to 62 MPa (about 32% difference). Moreover, according to Fig. 13(d), the 5% quantile of the ecdf for the difference between the VHCF strength is 3.5. A difference equal to 0 corresponds to the 2.7% quantile of the ecdf. Therefore, this analysis confirms that, with a confidence level larger than 95%, the powder size significantly affects the VHCF response and that the fatigue strength at $N = 10^9$ cycles decreases by reducing the powder size.

5. Conclusions

In this paper, the VHCF property and crack initiation characteristics of SLM-manufactured AlSi10Mg specimens with different printing powder sizes were investigated through a series of experiments. The main conclusions are as follows:

(1) The elongation of Group B (powder size 50 μm) is much higher than that of Group A (powder size 20 μm). This is because that, with the decrease of powder size, the number of defects increases and the resulted density decreases.
(2) The fatigue performance of Group B is superior to Group A.
(3) Group A contains a relatively larger number of defects than Group B, which cause a part of crack initiation of Group A from specimen surface in VHCF regime. Unmelted powders are the main cause of crack initiation. Group B is more likely to feature subsurface or internal crack initiation in VHCF regime.
(4) The specimens printed with a powder size of 20 μm are characterized by a significantly smaller VHCF strength at $N = 10^9$ cycles. The median VHCF strength is reduced by 32%, if the powder size decreases from 50 μm to 20 μm. Moreover, with a confidence level larger than 95%, the powder size significantly affects the VHCF response: the smaller the powder size, the smaller the VHCF strength.

Declaration of Competing Interest

The authors declare that they have no known competing financial interests or personal relationships that could have appeared to influence the work reported in this paper.

Acknowledgement

This work was funded by the NSFC Basic Science Center Program for "Multiscale Problems in Nonlinear Mechanics" (No.11988102), the National Natural Science Foundation of China (No. 11872364, 11932020, 12072345), and CAS Pioneer Hundred Talents Program.

References

[1] Wang Z, Wu W, Qian G, Sun L, Lia X, Correia J. In-situ SEM investigation on fatigue behaviors of additive manufactured Al-Si10-Mg alloy at elevated temperature. Eng Fract Mech 2019;214:149–63.
[2] Yadollahi A, Shamsaei N. Additive manufacturing of fatigue resistant materials: Challenges and opportunities. Int J Fatigue 2017;98:14–31.
[3] Herzog D, Seyda V, Wycisk E, Emmelmanna C. Additive manufacturing of metals. Acta Mater 2016;117:371e392.
[4] Zhang Y, Wu L, Guo X, Kane S, Deng Y, Jung Y, et al. Additive Manufacturing of Metallic Materials: A Review. J Mater Eng Performance 2018;27:1–13.
[5] Gorsse S, Hutchinson C, Gouné M, Banerjee R. Additive manufacturing of metals: a brief review of the characteristic microstructures and properties of steels, Ti-6Al-4V and high-entropy alloys. Sci Tech Adv Mater 2017;18:584–610.
[6] Martin J, Yahata B, Hundley J, Mayer J, Schaedler T, Pollock T. 3D printing of high-strength aluminium alloys. Nature 2017;549:365–9.
[7] Tradowsky U, White J, Ward R, Read N, Reimers W, Attallah M. Selective laser melting of AlSi10Mg: Influence of post-processing on the microstructural and tensile properties development. Mater Des 2016;105:212–22.
[8] Günther J, Krewerth D, Lippmann T, Leuders S, Tröster T, Weidner A, et al. Fatigue life of additively manufactured Ti–6Al–4V in the very high cycle fatigue regime. Int J Fatigue 2017;94:236–45.
[9] Tridello A, Biffi C, Fiocchi J, Bassani P, Chiandussi G, Rossetto M, et al. VHCF response of as-built SLM AlSi10Mg specimens with large loaded volume. Fatigue Fract Eng Mater Struct 2018;41:1918–28.
[10] Tridello A, Fiocchi J, Biffi C, Chiandussi G, Rossetto M, Tuissi A, et al. Influence of the annealing and defects on the VHCF behavior of an SLM AlSi10Mg alloy. Fatigue Fract Eng Mater Struct 2019;42:2794–807.
[11] Jeddi D, Palin-Luc T. A review about the effects of structural and operational factors on the gigacycle fatigue of steels. Fatigue Fract Eng Mater Struct 2018;41:969–90.
[12] Naito T, Ueda H, Kikuchi M. Fatigue behavior of carburized steel with internal oxides and nonmartensitic microstructure near the surface. Metall Mater Trans A 1984;15:1431–6.
[13] Nishijima S, Kanazawa K. Stepwise S-N curve and fish-eye failure in gigacycle fatigue. Fatigue Fract Eng Mater Struct 1999;22:601–7.
[14] Fan J, McDowell D, Horstemeyer M, Gall K. Cyclic plasticity at pores and inclusions in cast Al–Si alloys. Eng Fract Mech 2003;70:1281–302.
[15] Hong Y, Lei Z, Sun C, Zhao A. Propensities of crack interior initiation and early growth for very-high-cycle fatigue of high strength steels. Int J Fatigue 2014;58:144–51.
[16] Bagehorn S, Wehr J, Maier H. Application of mechanical surface finishing processes for roughness reduction and fatigue improvement of additively manufactured Ti-6Al-4V parts. Int J Fatigue 2017;102:135–42.
[17] Hong Y, Liu X, Lei Z, Sun C. The formation mechanism of characteristic region at crack initiation for very-high-cycle fatigue of high-strength steels. Int J Fatigue 2016;89:108–18.
[18] Chandran KS. A physically based universal functional to characterize the mechanism of fatigue crack growth in materials. Scripta Mater 2015;107:115–8.
[19] Murakami Y, Nomoto T, Ueda T. On the mechanism of fatigue failure in the superlong life regime (N>10^7 cycles). Part I: influence of hydrogen trapped by inclusions. Fatigue Fract Eng Mater Struct 2000;23:893–902.
[20] Beretta S, Romano S. A comparison of fatigue strength sensitivity to defects for materials manufactured by AM or traditional processes. Int J Fatigue 2017;94:178–91.
[21] Zhao A, Xie J, Sun C, Lei Z, Hong Y. Prediction of threshold value for FGA formation. Mater Sci Eng A 2011;528:6872–7.
[22] Pan X, Hong Y. High-cycle and very-high-cycle fatigue behaviour of a titanium alloy with equiaxed microstructure under different mean stresses. Fatigue Fract Eng Mater Struct 2019;42:1950–64.
[23] Qian G, Zhou C, Hong Y. Experimental and theoretical investigation of environmental media on very-high-cycle fatigue behavior for a structural steel. Acta Mater 2011;59:1321–7.
[24] Tridello A, Qian G, Li Y, Paolino D, Berto F, Hong Y. Very-high-cycle fatigue behavior of Ti-6Al-4V manufactured by selective laser melting: Effect of build orientation. Int J Fatigue 2020;136:105628.
[25] Qian Y, Qian G, Jian Z, Pan X, Ma X, Hong Y. Very-high-cycle fatigue behavior of AlSi10Mg manufactured by selective laser melting: Effect of build orientation and mean stress. Int J Fatigue 2020;138:105696.
[26] Srinivasa R, Rajaa A, Priyanka N, Jayaganthana R, Vasaa N. Influence of working environment and built orientation on the tensile properties of selective laser melted AlSi10Mg alloy. Mater Sci Eng A 2019;750:141–51.
[27] Uzan N, Ramati S, Shneck R, Frage N, Yeheskel O. On the effect of shot-peening on fatigue resistance of AlSi10Mg specimens fabricated by additive manufacturing using selective laser melting (AMSLM). Additive Manufact 2018;21:458–64.
[28] Aboulkhair N, Everitt N, Ashcroft I, Tuck C. Reducing porosity in AlSi10Mg parts processed by selective laser melting. Additive Manufact 2014;1–4:77–86.
[29] Hirata T, Kimura T, Nakamoto T. Effects of hot isostatic pressing and internal porosity on the performance of selective laser melted AlSi10Mg alloys. Mater Sci Eng A 2020;772:138713.
[30] Domfang Ngnekou J, Nadot Y, Henaff G, Nicolai J, Ridosz L. Influence of defect size on the fatigue resistance of AlSi10Mg alloy elaborated by selective laser melting (SLM). Proc Struct Int 2017;7:75–83.
[31] Uzan N, Shneck R, Yeheskel O, Frage N. High-temperature mechanical properties of AlSi10Mg specimens fabricated by additive manufacturing using selective laser melting technologies (AMSLM). Additive Manufact 2018;24:257–63.
[32] Rosenthal I, Stern A, Frage N. Strain rate sensitivity and fracture mechanism of AlSi10Mg parts produced by Selective Laser Melting. Mater Sci Eng A 2017;682:509–17.
[33] Read N, Wang W, Essa K, Attallah M. Selective laser melting of AlSi10Mg alloy: Process optimisation and mechanical properties development. Mater Des 2015;65:417–24.
[34] Bastien V, Nicolas S. Numerical modelling of surface roughness effect on the fatigue behavior of Ti-6Al-4V obtained by additive manufacturing. Int J Fatigue 2019;123:180–95.

[35] Victor C, Philippe Q. Comparative study of fatigue properties of Ti-6Al-4V specimens built by electron beam melting (EBM) and selective laser melting (SLM). Mater Charact 2018;143:76–81.
[36] Dzugan J, Seifib M. Effects of thickness and orientation on the small scale fracture behaviour of additively manufactured Ti-6Al-4V. Mater Charact 2018;143:94–109.
[37] Beevers E, Brandão A, Gumpinger J, Gschweitl M, Seyfert C, Hofbauer P, et al. Fatigue properties and material characteristics of additively manufactured AlSi10Mg-Effect of the contour parameter on the microstructure, density, residual stress, roughness and mechanical properties. Int J Fatigue 2018;117:148–62.
[38] Han Q, Yang J. Effect of heat treatment and laser surface remelting on AlSi10Mg alloy fabricated by selective laser melting. Int J Adv Manuf Tech 2019;102:3315–24.
[39] Leung A, Marussi S, Atwood R, Towrie M, Withers P, Lee P. In situ X-ray imaging of defect and molten pool dynamics in laser additive manufacturing. Nature Commu 2018;9:1355.
[40] Xiong Z, Liu S, Lia S, Shi Y, Yang Y, Misrad R. Role of melt pool boundary condition in determining the mechanical properties of selective laser melting AlSi10Mg alloy. Mater Sci Eng A 2019;740–741:148–56.
[41] Paolino D, Chiandussi G, Rossetto M. A unified statistical model for S-N fatigue curves: probabilistic definition. Fatigue Fract Eng Mater Struct 2013;36:187–201.
[42] Lore T, Karolien K, Jean-Pierre K, Jan VH. Fine-structured aluminum products with controllable texture by selective laser melting of pre-alloyed AlSi10Mg powder. Acta Mater 2013;61:1809–19.
[43] Witkin D, Patel D, Bean G. Notched fatigue testing of Inconel 718 prepared by selective laser melting. Fatigue Fract Eng Mater Struct 2019;42:166–77.
[44] Romano S, Patriarca L, Foletti S, Beretta S. LCF behaviour and a comprehensive life prediction model for AlSi10Mg obtained by SLM. Int J Fatigue 2018;117:47–62.
[45] Cai C, Gao X, Teng Q. A novel hybrid selective laser melting/hot isostatic pressing of near-net shaped Ti-6Al-4V alloy using an in-situ tooling: Interfacial microstructure evolution and enhanced mechanical properties. Mater Sci Eng A 2018;717:95–104.
[46] Qian G, Jian Z, Pan X, Berto F. In-situ investigation on fatigue behaviors of Ti-6Al-4V manufactured by selective laser melting. Int J Fatigue 2020;133:105424.
[47] Lua J, Ling C. In-situ investigation of the anisotropic mechanical properties of laser direct metal deposition Ti6Al4V alloy. Mater Sci Eng A 2018;712:199–205.
[48] Walker K, Liu Q. Evaluation of fatigue crack propagation behaviour in Ti-6Al-4V manufactured by selective laser melting. Int J Fatigue 2017;104:302–8.
[49] Du Plessis A, Beretta S. Killer notches: The effect of as-built surface roughness on fatigue failure in AlSi10Mg produced by laser powder bed fusion. Additive Manufact 2020;35:101424.
[50] Aboulkhair T, Maskery I, Tuck C, Ashcroft I, Everitt N. Improving the fatigue behaviour of a selectively laser melted aluminum alloy: Influence of heat treatment and surface quality. Mater Des 2016;104:174–82.
[51] Weingarten C, Buchbinder D, Pirch N, Meiners W, Wissenbach K, Poprawe R. Formation and reduction of hydrogen porosity during selective laser melting of AlSi10Mg. J Mater Process Tech 2015;221:112–20.
[52] Strumza E, Hayun S, Barzilai S, Finkelstein Y, David R, Yeheskel O. In situ detection of thermally induced porosity in additively manufactured and sintered objects. J Mater Sci 2019;54:8665–74.
[53] Liu Y, Chen S, Tian R, Wang Q. Design of dog-bone-shaped ultrasonic vibrational fatigue specimen and its application in study on VHCF behavior of 6063 aluminium alloy. Adv Mater Res 2011;160–162:783–8.
[54] Hu Y, Wu S, Withers P, Zhang J, Bao H, Fu Y, et al. The effect of manufacturing defects on the fatigue life of selective laser melted Ti-6Al-4V structures. Mater Des 2020;192:108708.
[55] Murakami Y. Metal Fatigue: Effects of Small Defects and Nonmetallic Inclusions. Tokyo: Yokendo Ltd.; 1993.
[56] Murakami Y. Material defects as the basis of fatigue design. Int J Fatigue 2012;41:2–10.
[57] Paolino D, Tridello A, Chiandussi G, Rossetto M. Statistical estimation of duplex S-N curves. Key Eng Mater 2016;664:285–94.
[58] Paolino D, Tridello A, Chiandussi G, Rossetto M. S-N curves in the very-high-cycle fatigue regime: statistical modeling based on the hydrogen embrittlement consideration. Fatigue Fract Eng Mater Struct 2016;39:1319–36.
[59] Smith K. A stress-strain function for the fatigue of metals. J Mater 1970;5:767–78.